


RESEARCH ARTICLE | SEPTEMBER 19 2023

Continuous beam steering with a varactor-based reconfigurable intelligent surface in the Ka-band at 31 GHz

Alexander Wolff ; Lars Franke; Steffen Klingel; Janis Krieger; Lukas Mueller; Ralf Stemler; Marco Rahm

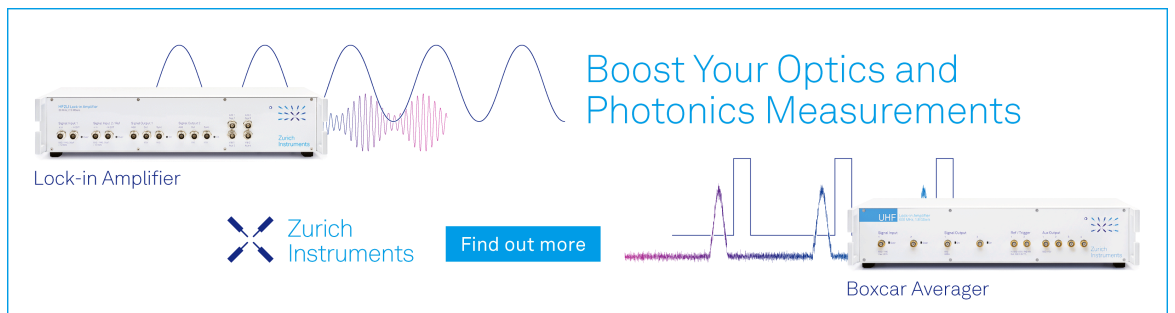


J. Appl. Phys. 134, 114502 (2023)


<https://doi.org/10.1063/5.0168330>



Boost Your Optics and Photonics Measurements



Lock-in Amplifier

 Zurich Instruments

[Find out more](#)

Boxcar Averager

Continuous beam steering with a varactor-based reconfigurable intelligent surface in the Ka-band at 31 GHz

Cite as: J. Appl. Phys. **134**, 114502 (2023); doi: [10.1063/5.0168330](https://doi.org/10.1063/5.0168330)

Submitted: 18 July 2023 · Accepted: 30 August 2023 ·

Published Online: 19 September 2023



Alexander Wolff,^{a)}  Lars Franke, Steffen Klingel, Janis Krieger, Lukas Mueller, Ralf Stemler, and Marco Rahm

AFFILIATIONS

Department of Electrical and Computer Engineering, RPTU Kaiserslautern-Landau, and Research Center OPTIMAS, D-67663 Kaiserslautern, Germany

^{a)}Author to whom correspondence should be addressed: alexander.wolff@rptu.de

ABSTRACT

Varactor diodes have been proposed as active tuning elements of reconfigurable metasurfaces in the Ka-band. However, their experimental realization in this frequency range has not been demonstrated yet. We report the implementation of such a reconfigurable intelligent surface (RIS) made of 20×20 unit cells. By active tuning of the bias voltage of the varactors, the phase of the backward diffracted wave can be continuously tuned between 0° and 180° . Thus, the phase tuning can be independently controlled for each unit cell. The frequency working range of the RIS is 1.1 GHz (from 30.6 to 31.7 GHz). As an illustration of the practical use, we demonstrate continuous beam steering of microwave radiation at 31 GHz in a defined propagation plane.

© 2023 Author(s). All article content, except where otherwise noted, is licensed under a Creative Commons Attribution (CC BY) license (<http://creativecommons.org/licenses/by/4.0/>). <https://doi.org/10.1063/5.0168330>

I. INTRODUCTION

A reconfigurable intelligent surface (RIS) is a dynamic metasurface consisting of unit cells that incorporate one or more active elements for the purpose of modifying their electromagnetic characteristics. By individual tuning on the unit cell level, a reconfigurable spatial pattern of complex surface impedances can be created that allows both, local and global control over the spatial phase of a diffracted wave from the RIS. As a result, diffraction from an RIS can be used to control the propagation of an electromagnetic wave at will, as, for example, in beam focusing or beam steering. For this reason, RISs have been proposed as beam forming components in 5G and 6G mobile communication^{1,2} and for radar cross-section (RCS) reduction.³

In this context, RISs in the literature differ fundamentally with respect to the specific tuning elements employed for reconfiguring their surface impedance. While CMOS components, graphene electronics, and micro-electro-mechanical systems (MEMS) have proven to serve as reliable tuning elements in RISs for working frequencies in the terahertz range,⁴⁻⁷ PIN diodes have been the preferred means of choice in RISs up to 60 GHz.⁸⁻¹⁰

However, there are two main drawbacks associated with the use of PIN diodes. First, the embedding of PIN diodes in a RIS only allows for discrete shifting in the phase of the diffracted wave at the unit cell level, specifically by either 0° or 180° . In such a digital RIS coding scheme, the degrees of freedom for beam steering are inherently limited. Second, since the impedance of the PIN diodes is tuned by application of a forward bias voltage, the resulting currents and power consumption are significant, especially when more than one PIN diode is used per unit cell.^{3,11} In contrast to PIN diodes, varactor diodes are mostly operated at a reverse bias voltage, which keeps the currents and power consumption extremely low. In consequence, an increase in the amount of used varactor diodes per unit cell comes at a lower increase in the cost of operation. Furthermore, the capacitance, and, thus, the complex impedance of varactor diodes, can be continuously tuned and is not restricted to discrete values. Consequently, the use of varactor diodes as adjustable components substantially enhances the flexibility of the tuning process, thereby increasing the level of freedom in beamforming applications.

So far however, varactor diodes have only been demonstrated to be effective on RISs operating in the single-digit gigahertz frequency

29 April 2024 13:45:21

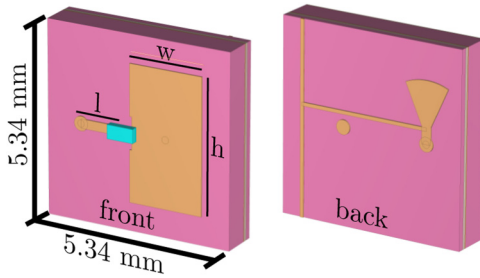


FIG. 1. Front side (left) and back side (right) of the unit cell of the RIS. The orange structures are made of copper. The pink board represents the RO4350B substrate. The cyan-colored box indicates the varactor diode. The dimensions of the copper antenna are $h = 3.77$ mm, $w = 2.1$ mm, and $l = 1.28$ mm.

range.^{12–14} Apart from that, their usage as tuning elements in the K-band and above has been merely theoretically hypothesized,^{15,16} but not experimentally demonstrated. Here, we report and discuss the experimental implementation of a varactor-based RIS operating in the Ka-band at 31 GHz. Besides a profound theoretical and experimental analysis of the electromagnetic properties of the tunable RIS, we also apply capacitive tuning of the varactor diodes for continuous beam steering in a defined diffraction plane.

II. RIS DESIGN

The designed RIS has been manufactured by standard printed circuit board (PCB) fabrication technology. The unit cell of the RIS and the associated geometrical dimensions are illustrated in Fig. 1. The three $35\ \mu\text{m}$ thick copper layers are spaced by two Rogers RO4350B substrates with thicknesses of 760 and $270\ \mu\text{m}$, respectively. The top layer of the RIS carries patch antennas with varactor diodes for active capacitive tuning. The unit cell has a width and height of approximately $\lambda/2$ with respect to the wavelength λ of the microwave radiation. The working frequency of the structure is 31 GHz. The second layer of the PCB is a ground plane that is connected to the center of the patch antenna through a via. It also serves as the ground potential for the bias voltage of the varactor

diode. The varactor DC bias voltage is applied through a separate via that is not electrically connected to the ground plane. The bottom layer of the RIS hosts a radial stub for each unit cell to insulate the DC feed line from the microwave. The DC feed lines of all unit cells are vertically connected. As a result, all unit cells in one of the 20 columns of the RIS are switched with the same bias voltage from an operational amplifier, which implies the ability for beam steering in a specified plane. We refer to this plane as a horizontal plane in the remainder of the text. The cyan-colored box in Fig. 1 indicates the varactor diode (MACOM MAVR-011020-1411). The patch antenna of the unit cell has been analytically laid out as described in Ref. 17, and the unit cell structure has been numerically optimized in CST Studio Suite.

The fabricated RIS is shown in Fig. 2(a). It consists of 20×20 unit cells and a blank, two unit cells wide border around the perimeter. The total aperture of the RIS is $128 \times 128\ \text{mm}^2$.

III. RIS CHARACTERIZATION

We experimentally characterized the electromagnetic properties of the RIS by measuring the electric field distribution of the back-diffracted wave from the RIS in a microwave goniometer [see Fig. 2(b)]. The goniometer was located in an anechoic chamber to avoid parasitic scattering from the boundaries. In a first step, we evaluated the relationship between the phase shift in the back-diffracted wave and the applied reverse bias voltage to the varactor diodes in the RIS unit cells. In this initial measurement of the S_{11} scattering parameter, we applied identical bias voltages to all columns and, thus, to all unit cells in the RIS during the tuning process. In order to avoid shadowing by the receiving antenna, we inclined the RIS by 15° (measured between the RIS normal and the horizontal plane) such that the backward diffraction occurred in a plane at an inclination angle of 30° .

Figures 3(b) and 3(a) show the magnitude and the relative phase of the S_{11} scattering parameter for a frequency range from 19 to 33 GHz when the bias voltage is tuned from -20 to $+10$ V uniformly for all unit cells. Please note that the linear magnitude of the S_{11} scattering parameter has been normalized to the maximum value obtained in Fig. 3(b), while the phase in Fig. 3(a) has been plotted relative to the measured reference phase at a bias voltage of

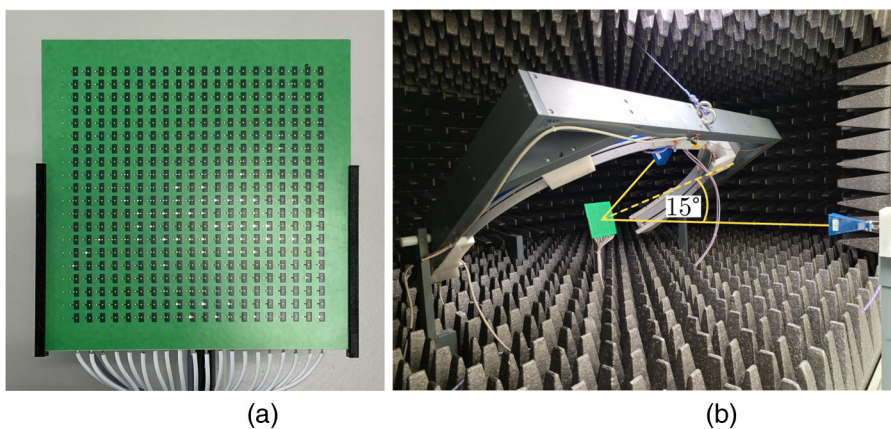


FIG. 2. (a) Front side of the RIS. The aperture of the RIS is $128 \times 128\ \text{mm}^2$. (b) Goniometer and RIS at a 15° inclination angle inside an anechoic chamber.

29 April 2024 13:45:21

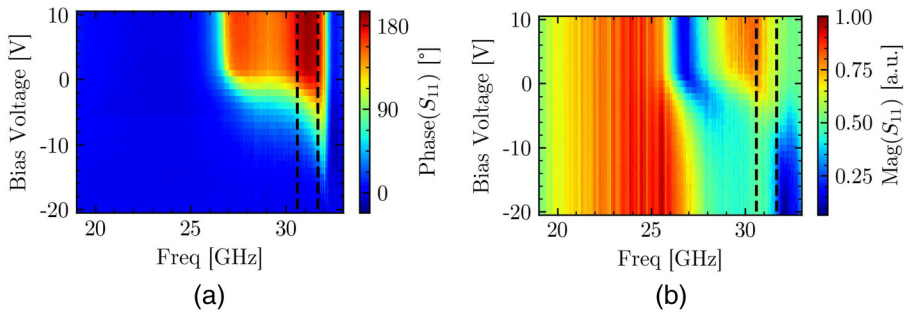


FIG. 3. Phase (a) and magnitude (b) in the maximum of the mainlobe of the backward diffracted wave plotted vs frequency and bias voltage. The phase is measured relative to the reference phase at a bias voltage of -20 V. The linear magnitude is normalized to the maximum value in the plot. The dashed black lines illustrate the frequency range, in which the phase difference can be tuned at least between 0° and 180° .

-20 V. The voltage drop was measured across a series circuit of the corresponding varactor diode and a resistor with a resistance of 910Ω . The measurements show that, for a frequency range between 30.6 and 31.7 GHz, the phase of the S_{11} -parameter could be continuously tuned from 0° to 180° by changing the bias voltage from -20 to $+10$ V. This corresponds to a working frequency bandwidth of 1.1 GHz, which is indicated by the black dashed lines in Fig. 3. Within this tuning range, the magnitude of S_{11} varied between 0.25 and 0.86 a.u. However, we also observed empirically that a phase difference of up to 160° between unit cells is sufficient for effective beam steering in a defined plane. In this case, the corresponding phase shift in the S_{11} scattering parameter can be obtained in a frequency domain between 30.0 and 31.9 GHz, which implies an increased working frequency bandwidth of 1.9 GHz. In this tuning range, the S_{11} scattering parameter changed from 0.15 to 0.87 a.u.

As specific examples, Fig. 4 depicts the dependence of the phase and magnitude of S_{11} on the applied bias voltage for working frequencies at 30.6 , 31.0 , and 31.6 GHz. These curves have been obtained by evaluating the S_{11} phase and magnitude in Figs. 3(a) and 3(b) at the respective frequencies. As can be seen, the S_{11} magnitude increases from 0.43 to 0.71 a.u. and the S_{11} phase changes between 0° and 180° , when the bias voltage is tuned from -20 to $+10$ V. By using the measured frequency dependence of the complex S_{11} scattering parameter as a calibration curve, it was possible to assign phase values between 0° and 180° to each RIS column and, thus, to create arbitrary, column-wise organized, spatial phase patterns. As an illustrative application, we utilized column-wise phase tuning on the RIS to implement beam steering of microwaves at 31 GHz in a defined plane, as described in Sec. IV.

IV. CONTINUOUS BEAM STEERING AT 31 GHz IN A DEFINED PLANE

In contrast to RISs with binary switching elements,^{8–10} varactor-equipped RISs can diffract incident waves to a continuous range of deflection angles. Since our RIS implementation was limited to a column-wise address of the embedded varactors that did not allow individual control over each unit cell, we could not continuously steer a normally incident wave only in a defined plane. For continuous beam steering within the whole hemisphere, individual control over the bias voltage in each unit cell is mandatory, which sophisticates the routing and the RIS design considerably.

For this reason, two-dimensional beam steering has not been considered in this publication.

For implementation of the RIS beam steerer, we first determined the required phase switching patterns to achieve continuous tuning of the deflection angle of the back-diffracted waves. We selected a frequency of 31 GHz as the operational frequency for the RIS. We assumed that the wave was normally incident before being deflected by the RIS. For optimization, we used particle swarm optimization to maximize the electric field of the deflected wave for any desired deflection angle. The method for calculating the electric field distribution was described in an earlier work.¹⁸ The column-wise phase switching patterns, which result from the optimization, are shown in Table I. We used the calibration curve depicted in Fig. 4 to determine the necessary bias voltage pattern for a given phase pattern at 31 GHz.

As in the previous experiment, the RIS was tilted by an angle of 15° , measured between the RIS normal and the horizontal plane of the experimental setup to avoid masking of the receiving antenna. As a result, the backward diffraction and, thus, the beam steering occurred within a plane that was tilted by 30° with respect to the horizontal. Since the mainlobe of the back-diffracted wave had a FWHM of more than 7° within the deflection plane for all phase patterns, we measured the beam steering with an angle resolution of 5° . The microwave frequency of the incident wave was 31 GHz.

Figures 5(a) and 5(b) show polar plots of the calculated (following the procedure in Ref. 18) and measured electric field

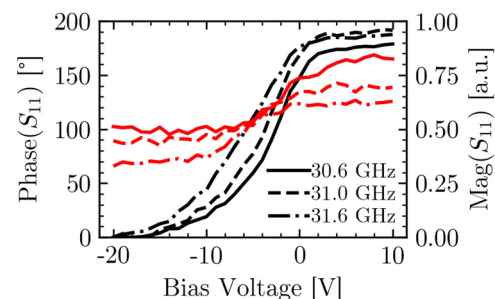
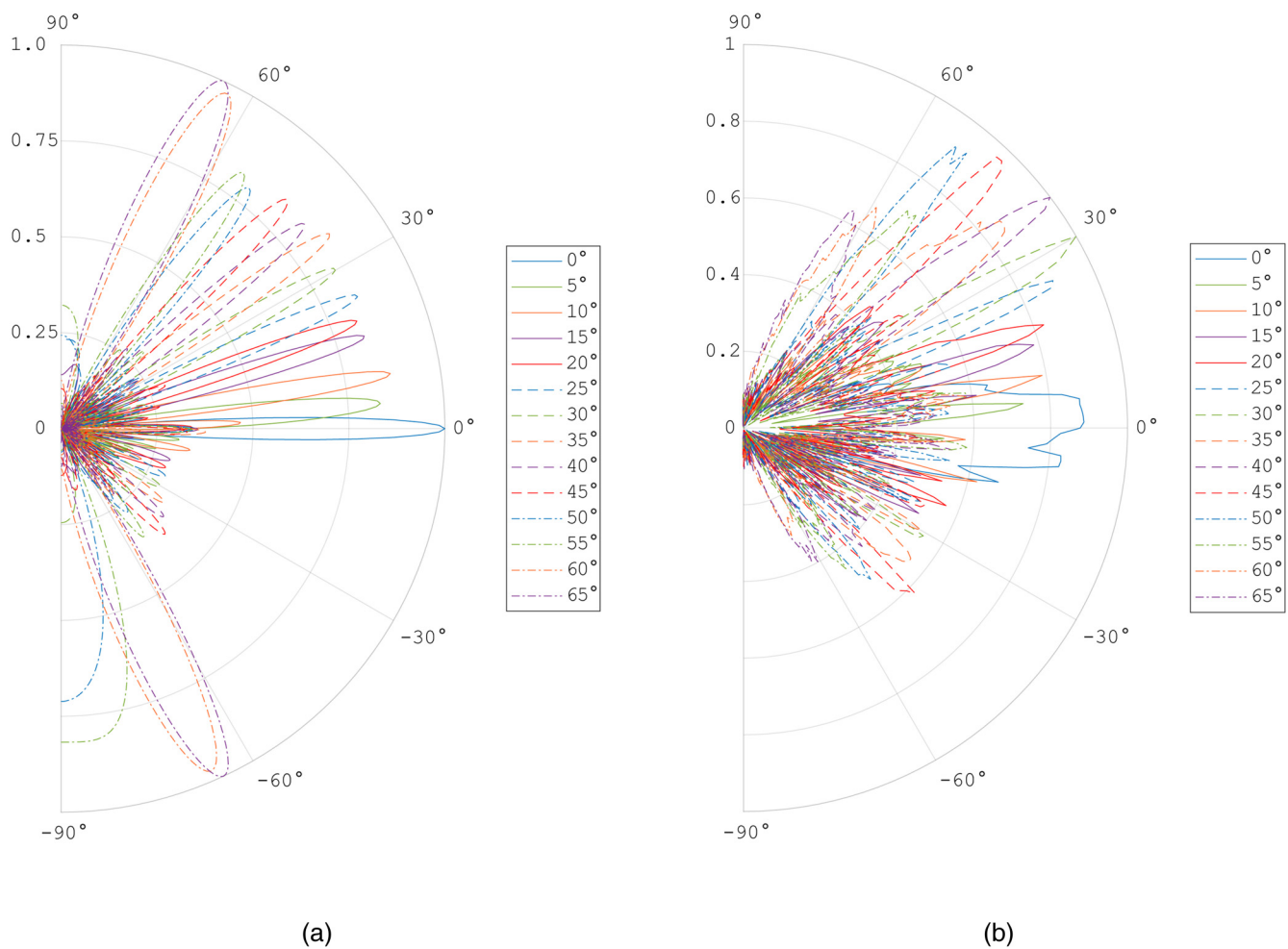


FIG. 4. Phase (black) and magnitude (red) of the measured S_{11} scattering parameter at different frequencies plotted vs the bias voltage.

29 April 2024 13:45:21

TABLE I. Calculated phase patterns for the beam steering RIS. The left column displays the target deflection angle. The remaining 20 columns represent the columns of the RIS and list the phase in each column that was determined to achieve the desired deflection angle.

Deflection angle	RIS column number																			
	01	02	03	04	05	06	07	08	09	10	11	12	13	14	15	16	17	18	19	20
0°	180°	180°	180°	180°	180°	180°	180°	180°	180°	180°	180°	180°	180°	180°	180°	180°	180°	180°	180°	180°
5°	180°	180°	0°	0°	0°	0°	0°	11°	28°	46°	63°	80°	97°	115°	132°	149°	167°	180°	180°	180°
10°	0°	0°	11°	46°	80°	115°	149°	180°	180°	180°	0°	0°	0°	31°	65°	100°	134°	169°	180°	180°
15°	39°	97°	155°	180°	0°	0°	27°	85°	143°	180°	180°	0°	16°	74°	132°	180°	180°	0°	4°	62°
20°	41°	108°	176°	180°	0°	20°	88°	156°	180°	0°	0°	68°	136°	180°	0°	0°	48°	116°	180°	180°
25°	83°	164°	180°	0°	46°	127°	180°	0°	9°	90°	171°	180°	0°	53°	134°	180°	0°	16°	97°	178°
30°	120°	180°	0°	58°	157°	180°	0°	95°	180°	0°	33°	133°	180°	0°	71°	170°	0°	9°	108°	180°
35°	31°	144°	180°	12°	126°	180°	0°	108°	180°	0°	90°	180°	0°	72°	180°	0°	54°	168°	0°	36°
40°	50°	177°	0°	73°	180°	0°	96°	180°	0°	119°	180°	14°	142°	180°	38°	165°	0°	61°	180°	0°
45°	180°	0°	116°	180°	37°	178°	0°	99°	180°	20°	160°	0°	81°	180°	2°	143°	0°	64°	180°	0°
50°	0°	87°	180°	40°	180°	0°	150°	0°	103°	180°	56°	180°	9°	166°	0°	119°	0°	72°	180°	25°
55°	164°	0°	129°	0°	95°	180°	60°	180°	26°	180°	0°	154°	0°	120°	0°	85°	180°	51°	180°	16°
60°	180°	39°	180°	30°	180°	21°	180°	11°	180°	2°	178°	0°	169°	0°	159°	0°	150°	0°	141°	0°
65°	0°	180°	0°	180°	0°	180°	0°	180°	0°	180°	0°	180°	0°	180°	0°	180°	0°	180°	0°	180°



29 April 2024 13:45:21

FIG. 5. Polar plots of the (a) calculated electric far field and the (b) measured electric far field of the back-diffracted waves from the RIS. The curves are labeled according to their target deflection angles.

distributions of the back-diffracted waves from the RIS for all deflection angles listed in Table 1. The curves are appropriately labeled according to the desired deflection angle. The electric field distributions are normalized to the maximum peak value in the respective graph. The measured electric field amplitude was above 0.5 a.u. for all deflection angles between 0° and 65° .

A comparison between the calculated far field and the measured electric field of the back-diffracted wave evidences that the mainlobe of the steered beam occurred at the expected deflection angles, with a maximum deviation of 3° at deflection angles of 35° and 40° . However, this offset can be partly attributed to the systematic errors in repeated measurements by the goniometer that restrict the angle resolution to $\pm 1^\circ$. Furthermore, the aperture of the receiving horn antenna in the specified measurement plane is 32.8 mm wide, which results in integration of the electric field over an opening angle of 3.8° in this plane.

In addition to the electric field mainlobes, we also observed several sidelobes that were not expected in the calculated far fields. We attribute the occurrence of additional sidelobes to the fact that the distance between the receiving antenna and RIS was only 0.5 m, which implies that we measured the electric field of the back-diffracted wave in the near-field and not in the far field. To support this hypothesis, we calculated the electric near-field distribution of the diffracted wave with the Kirchhoff diffraction formula under consideration of the geometry in our goniometer.¹⁹ The resulting electric near-field distribution for a deflection angle of 25° is shown as an example in the polar plot of Fig. 6, alongside with the corresponding calculated far field and the measured electric field. Note that the measured electric field in Fig. 6 was normalized to its maximum value, in contrast to the electric far fields in Fig. 5(b) that were normalized to the global maximum of all displayed distributions. The arrows in Fig. 6 indicate areas, where the measured

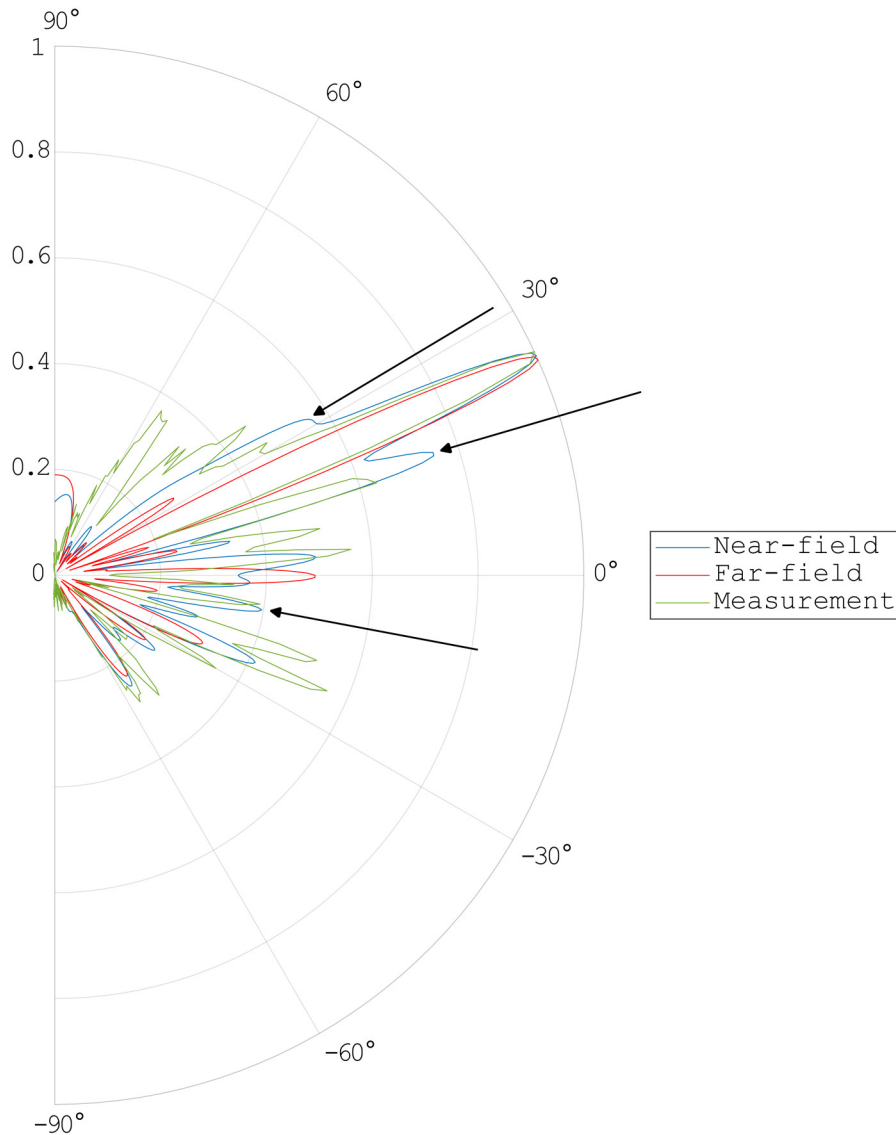


FIG. 6. Calculated electric near-field (blue), calculated far field (red), and measured electric field (green) of the back-diffracted wave from the RIS for a target deflection angle of 25°.

electric field pattern exhibits closer resemblance to the calculated near-field distribution than the far-field distribution.

V. CONCLUSION

We successfully designed and implemented a varactor-based RIS, capable of achieving continuous phase tuning ranging from 0° to 180° at the unit cell level. In order to achieve a relative phase shift of 180° in a unit cell, we changed the bias voltage from +10 to -20 V. The full phase shifting range could be established in a frequency working range from 30.6 to 31.7 GHz. In this publication, we applied the phase tuning column-wise, while, in principle, it can be applied individually and independently to each unit cell. As an exemplary application, we demonstrated beam steering of

microwaves at 31 GHz with a continuously tunable deflection angle from 0° to 65° in a defined plane.

ACKNOWLEDGMENTS

The authors acknowledge the financial support by the Federal Ministry of Education and Research of Germany in the project “Open6GHub” (Grant No. 16KISK004).

AUTHOR DECLARATIONS

Conflict of Interest

The authors have no conflicts to disclose.

29 April 2024 13:45:21

Author Contributions

Alexander Wolff: Investigation (equal); Writing – original draft (lead). **Lars Franke:** Conceptualization (equal); Formal analysis (equal). **Steffen Klingel:** Investigation (equal); Project administration (equal). **Janis Krieger:** Resources (equal). **Lukas Mueller:** Software (equal). **Ralf Stemler:** Resources (equal). **Marco Rahm:** Conceptualization (equal); Funding acquisition (equal); Supervision (equal).

DATA AVAILABILITY

The data that support the findings of this study are available from the corresponding author upon reasonable request.

REFERENCES

- ¹C. Pan, H. Ren, K. Wang, J. F. Kolb, M. Elkhassan, M. Chen, M. Di Renzo, Y. Hao, J. Wang, A. L. Swindlehurst, X. You, and L. Hanzo, “Reconfigurable intelligent surfaces for 6G systems: Principles, applications, and research directions,” *IEEE Commun. Mag.* **59**, 14–20 (2021).
- ²N. Kaina, M. Dupré, G. Lerosey, and M. Fink, “Shaping complex microwave fields in reverberating media with binary tunable metasurfaces,” *Sci. Rep.* **4**, 6693 (2014).
- ³T. J. Cui, M. Q. Qi, X. Wan, J. Zhao, and Q. Cheng, “Coding metamaterials, digital metamaterials and programmable metamaterials,” *Light: Sci. Appl.* **3**, e218 (2014).
- ⁴S. Venkatesh, X. lu, H. Saeidi, and K. Sengupta, “A high-speed programmable and scalable terahertz holographic metasurface based on tiled CMOS chips,” *Nat. Electron.* **3**, 785–793 (2020).
- ⁵X. Fu, F. Yang, C. Liu, X. Wu, and T. Cui, “Terahertz beam steering technologies: From phased arrays to field-programmable metasurfaces,” *Adv. Opt. Mater.* **8**, 1900628 (2020).
- ⁶J. Xu, W. Liu, and Z. Song, “Terahertz dynamic beam steering based on graphene coding metasurfaces,” *IEEE Photonics J.* **13**, 4600409 (2021).
- ⁷J. Kappa, D. Sokoluk, S. Klingel, C. Shemelya, E. Oesterschulze, and M. Rahm, “Electrically reconfigurable micromirror array for direct spatial light modulation of terahertz waves over a bandwidth wider than 1 THz,” *Sci. Rep.* **9**, 2597 (2019).
- ⁸X. Wan, Q. Xiao, Y. Z. Zhang, Y. Li, J. Eisenbeis, J. W. Wang, Z. A. Huang, H. X. Liu, T. Zwick, and T. J. Cui, “Reconfigurable sum and difference beams based on a binary programmable metasurface,” *IEEE Antennas Wirel. Propag. Lett.* **20**, 381–385 (2021).
- ⁹H. Kamoda, T. Iwasaki, J. Tsumochi, T. Kuki, and O. Hashimoto, “60-GHz electronically reconfigurable large reflectarray using single-bit phase shifters,” *IEEE Trans. Antennas Propag.* **59**, 2524–2531 (2011).
- ¹⁰J.-B. Gros, V. Popov, M. A. Odit, V. Lenets, and G. Lerosey, “A reconfigurable intelligent surface at mmwave based on a binary phase tunable metasurface,” *IEEE Open J. Commun. Soc.* **2**, 1055–1064 (2021).
- ¹¹L. Dai, B. Wang, M. Wang, X. Yang, J. Tan, S. Bi, S. Xu, F. Yang, Z. Chen, M. D. Renzo, C.-B. Chae, and L. Hanzo, “Reconfigurable intelligent surface-based wireless communications: Antenna design, prototyping, and experimental results,” *IEEE Access* **8**, 45913–45923 (2020).
- ¹²B. O. Zhu, J. Zhao, and Y. Feng, “Active impedance metasurface with full 360° reflection phase tuning,” *Sci. Rep.* **3**, 3059 (2013).
- ¹³M. Boyarsky, T. Sleasman, M. F. Imani, J. N. Gollub, and D. R. Smith, “Electronically steered metasurface antenna,” *Sci. Rep.* **11**, 4693 (2021).
- ¹⁴A. Araghi, M. Khalily, M. Safaei, A. Bagheri, V. Singh, F. Wang, and R. Tafazolli, “Reconfigurable intelligent surface (RIS) in the sub-6 GHz band: Design, implementation, and real-world demonstration,” *IEEE Access* **10**, 2646–2655 (2022).
- ¹⁵L. G. da Silva, Z. Chu, P. Xiao, and A. Cerqueira, “A varactor-based 1024-element RIS design for mm-waves,” *Front. Commun. Netw.* **4**, 1086011 (2023).
- ¹⁶H. Taghvaei, S. Abadal, A. Ptilakis, O. Tsilipakos, A. Tasolamprou, C. Liaskos, M. Kafesaki, N. Kantartzis, A. Cabello, and E. Alarcon, “Scalability analysis of programmable metasurfaces for beam steering,” *IEEE Access* **8**, 105320–105334 (2020).
- ¹⁷K. Kark, *Antennen und Strahlungsfelder: Elektromagnetische Wellen auf Leitungen, im Freiraum und ihre Abstrahlung* (Springer Fachmedien Wiesbaden, 2014).
- ¹⁸J. Kappa, Z. Dang, D. Sokoluk, and M. Rahm, “Analysis of coding metasurfaces for incident radiation at oblique incidence angles,” *OSA Continuum* **2**, 2172–2180 (2019).
- ¹⁹H.-H. Müller, *Meyers Physik-Lexikon* (Bibliographisches Institut, Fachredaktion für Naturwissenschaften und Technik, 1973).